2026 IEEE International Conference on Robotics and Automation (ICRA 2026)
June 1-5, 2026. Vienna, Austria

Increasing the Stiffness of Tendon-Driven Continuum Robots via Multi-Constraints

Zhenting Du[1,*], Xingyu Chen[1], Nikola Fischer[1], Weibang Bai[2], Quan Yuan[2], Bassel Zebian[3], Thomas Booth[1], Radhouene Neji[1], and Christos Bergeles[1]

***Abstract*— Increasing the stiffness of tendon-driven continuum robots for sufficient load-bearing ability without compromise in increasing tendon tension or limiting motion ability is a valuable yet challenging endeavor for safe and dexterous manipulation. To address this challenge, this paper proposes the concept of multiple constraints for tendon-driven continuum robots and investigates its capability in programmable stiffness strengthening. The concept introduces multiple tendon based constraints along the continuum structure, where all tendons can be actuated synchronized without exceeding the controllable degrees of freedom of conventional system. The schematic robot mechanism is given for the proposed concept, and the corresponding kinematic and static models are derived and verified. The ability of maintaining the tendon tension to the same level as the conventional system is illustrated using simulation. Implementing the proposed concept in a prototypical experimental robotic platform shows a stiffness improvement of up to 662% and a reduction in open loop kinematic control error of 34.5%.**

I. Introduction

Tendon-driven continuum robots (TDCRs) have demonstrated their dexterous motion abilities in a variety of domains, including minimally invasive surgery, narrow space inspection, and object manipulation [1] [2] [3]. Furthermore, they are sufficiently compliant for safe human-robot interaction [4]. The comparably low stiffness of their continuum structure, however, can lead to a limited load bearing capability. Their use for applications which require a larger stiffness are thus limited.

Tuning the stiffness of a TDCR to achieve an optimal balance between flexibility and load-bearing capacity for a specific task is an essential consideration for any robotic task which requires interaction with the surroundings, especially in uncertain environment [5]. The stiffness usually must be set during design and fabrication of the robot and cannot be altered afterwards, at least for a purely tendon-driven robot.

To address this limitation, various TDCR mechanisms have been investigated. One approach is to modify the stiffness of the TDCR backbone or restrict the relative motion between the components of the continuum structure. Examples include torsional stiffness-enhanced backbones [6] [7] and asymmetric rolling contact joints [8]. While the above methods examined the feasibility of permanent stiffness enhancement, they did not address the capacity for stiffness variability or accurate modeling of stiffening.

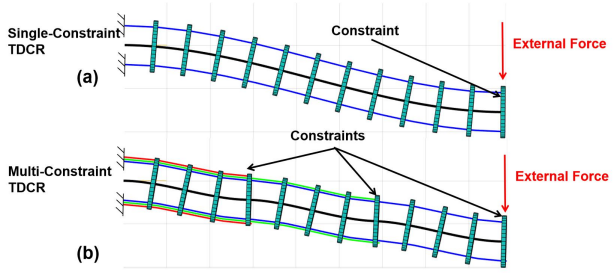

Fig. 1. Schematic shapes of single-constraint TDCR and multi-constraint TDCR subjected to external force. (a) The whole structure is deformed into a 'S' shape in the single-onstraint (conventional) TDCR. (b) The structure is deformed into several 'S' shapes in the proposed multi-constraint TDCR.

Several mechanisms for changing the stiffness of the backbone have also been investigated, e.g. vacuum jamming [9], shape memory alloys [10], shape memory polymers [11], rod locking [12], and low-melting-point alloys [13]. However, these methods require additional infrastructure close to the robot, thereby making the system larger and more complex and limiting the potential for miniaturization. Furthermore, TDCR with a stiffer backbone necessitates higher tendon tensions for actuation. This raises concerns about safety and structural integrity, as high tendon tension increases the risk of breakage and failure.

Other approaches focus on modifying the tendon-related mechanism to increase the system's stiffness. Oliever et al. demonstrated the ability of converging tendon routing to enhance stiffness [14]. Parsa et al. introduced extra pretensioned tendons in the robot body to increase stiffness [15]. Kim et al. investigated the variability in stiffness of a rolling contact joint with different tensions in the actuating tendons [16]. Cai et al. achieved tendon-based stiffening using spherical joints [17]. The stiffness could be calculated and controlled using a corresponding mathematical model. In the aforementioned studies, overall stiffness was achieved by increasing the tension in the actuating tendons. However, this still raises the risk of a critical tendon failure and elevates operational risks.

In this work, we propose the concept of multi-constraint

[1]School of Biomedical Engineering & Imaging Sciences, King's College London, UK. [2]ShanghaiTech Automation and Robotics (STAR) Center, School of Information Science and Technology, ShanghaiTech University, China. [3]Department of Neurosurgery, King's College Hospital NHS Trust, London, UK

Zhenting Du received support from the China Scholarship Council (CSC No.:202408310049). Additionally, the work was supported by EPSRC [EndoTheranostics / EP/Z003172/1, VITRRO / EP/Y024281/1] under the Horizon Europe Guarantee Extension, the Shanghai Pujiang Program (23PJ1408500), Shanghai Frontiers Science Center of Human-centered Artificial Intelligence (ShangHAI), and MoE Key Laboratory of Intelligent Perception and Human-Machine Collaboration (KLIP-HuMaCo).

*Corresponding author: Zhenting Du *(zhenting.du@kcl.ac.uk)*.

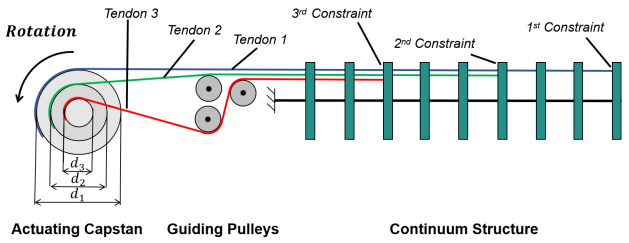

Fig. 2. Multi constraint concept for one exemplary actuator including a multi-diameter capstan, guide pulleys, and the continuum structure. The capstan, with concentric wheels of proportional diameters, synchronizes tendon movement, enabling actuation by a single motor. The constraints is named sequentially from furthest to nearest relative to the base.

for TDCR, as well as its corresponding kinematic and static models. Its minimalist design enables programmable adjustment of the structure's stiffness without compromising tendon tension or mobility.

II. Method and System Design

A TDCR usually consists of a flexible backbone with multiple spacer disks, through which a set of tendons is routed from the actuation unit to the distal end of a segment to achieve omnidirectional bending.

During asymmetric tendon motion, the robotic segment ideally bends into a circular arc with tendons attached at its tip. In practice, however, the shape of the continuum structure is also influenced by external forces and torques, e.g., due to its own weight and external loads or due to interaction with the environment. For example, the shape of the continuum robot is deformed from the initial straight state to an 'S' shape by the application of axial force when the robot is actuated by the tendon displacement. This is due to the orientation constraint at the tip introduced by the tendons due to the unchanged length of the tendon path.

Conversely, the tendon forces, together with the backbone's inherent stiffness, enable the robot to withstand deformations caused by external factors. However, this ability is limited when tendons are only attached at the tip of the continuum structure, as large deformation occurs along the body of the segment. The shape of the body can be determined mathematically by integrating along the segment using the orientation of its cross-section. A straightforward way to reduce deflection is to decrease the cross-sectional orientation of the segment along its integration path.

An novel and intuitive concept is proposed in this work to solve the deflection problem by using extra tendons to provide orientation constraints both at the tip and along the structure.

Fig. 1 shows a schematic comparison between a continuum robotic structure under external load at its distal tip with single constraint(a) and multi constraint(b). For the latter, six tendons are attached to three equally spaced constraints. In both examples the robot is initially straight and the tendon displacement is fixed. When a force is applied to the tip, the single-constraint continuum structure deforms into an 'S' shape. For the multi constraint, the constraints on the robot body keep the original orientation at these points. Thus, the S-shaped body is segmented and three shorter S-curves are formed between these constraints, promising to enhance the stiffness of the continuum structure.

For clarity, we distinguish between the tendons in the structure using the concepts of 'tendon sets' and 'tendon groups'. All tendons in the same tendon group have a parallel route and end at the same constraint position. Meanwhile, all tendons in the same tendon set have the same routing orientation angle, but end at different constraints along the segment. A constraint is generated when a group of tendons from different tendon sets attach to the same spacer disk.

similar structures, with tendons attached in the middle of the continuum structure, can be developed in the traditional TDCR system by integrating a single-segment structure into a multi-segment structure [18]. However, in the traditional TDCR system, each tendon requires an actuator. This introduces extra controllable degrees of freedom into the system, exceeding the concept of the minimum system unit. A major difference between multi-constraint and multi-segment TDCR is that the former proposes a novel actuation system, as shown in Fig. 2. In this system, a set of tendons can be actuated by one rotary actuator with a multi-diameter capstan.Therefore, the number of actuators remains the same as in the single-constraint system.

In general, the number and placement of constraint points can be varied, i.e., programmed. Furthermore, the stiffness can be changed during run-time by engaging or disengaging the constraint points.

A. Modeling Multi-Point Constrained TDCRs

For this work, the conventional TDCRs kinematic and static models are the basis that describe the novel multi-constraint concept.

1) Kinematic Model: The piecewise constant curvature model is utilized as a kinematic model, as has been proven efficient and accurate by previous research [19].

The forward kinematic model of the multi constraint TDCR is the same as the conventional TDCR, in which the tip position and orientation can be described as a function of the bending angle θ and bending plane angle φ as presented e.g. by [20]. Fig. 3 shows the schematic diagram of the shape of the continuum structure in the multi-constraint system, as well as a cross-section view of the structure for tendon identification. In a tendon set, the tendons $i = 1, 2, 3, \cdots, n$ are numbered from the one attached to the first constraint point at the tip to the last constraint point closer to the proximal end. The tendon groups $j = 1, 2, 3, \cdots, m$ are numbered counterclockwise around the origin from the x-axis.

For a segment tip bending angle θ and a bending plane angle φ, the displacement of each tendon ΔL_{ij} can be calculated as $\Delta L_{ij} = K_{ij} R_i \theta \cos(\alpha_j - \varphi)$, with $K_{ij} = L_{ij}/L_{total}$ being the ratio of the routing length of tendon L_i and that of the continuum structure L_1. R_i is the destance between tendon i in each set and backbone central line. For each set of tendons, considering that all tendons and

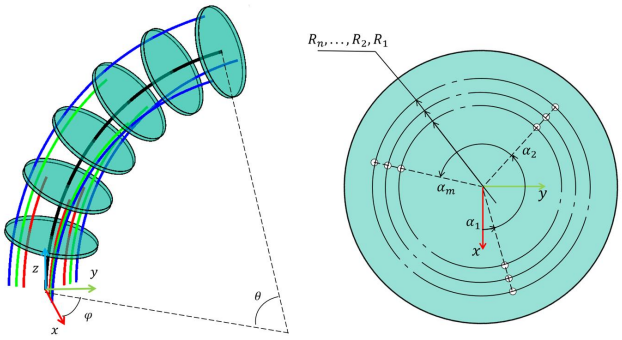

Fig. 3. Kinematic parameters of multi-constraint structure. (a) Segment bending angle and bending plan illustration (b) Cross-section view of the structure with tendon identification parameter

backbone are in the same plane, the ratio between the wheel of the tendon attached to the tip ($i = 1$) and the others of the tendons in the same set can be derived as

$$\frac{d_{ij}}{d_{1j}} = \frac{K_{ij}R_i\theta\cos(\alpha_j - \varphi)/q_j}{K_{1j}R_{1j}\theta\cos(\alpha_j - \varphi)/q_j} = \frac{\Delta L_{ij}}{\Delta L_{total}}, \quad (1)$$

where q_j is the actuating value, which is the angular displacement of the capstan attached with tendon set j, d_{ij} is the diameter of the wheel attached to tendon ij. This is the design criterion for the multi-diameter capstan to achieve the synchronized movement of the tendons in the same set.

For the inverse kinematic model, the mapping relation from tip position to the rotary actuation value is needed. Since each multi-point set of tendons is actuated by one actuator, in terms of simplification, only the displacement of the tip attached tendon is applied to derive the relation. q for each tendon set can be derived from

$$q_j = R_j\theta\cos(\alpha_j - \varphi)\frac{1}{d_j}, j = 1, 2, 3, \cdots, m \quad (2)$$

where R, and α, denote the distance from the central backbone to the routing of tendon, and the tendon routing position angle, respectively, and d_j is the capstan wheel diameter for the tip-attached tendon of the jth tendon set.

2) Static Model: For the static model, we assume that the continuum structure moves slowly, rendering dynamic effects such as inertia negligible.

The static model is based on Cosserat rod theory, which has been proven to be accurate for slender rod mechanisms [21]. It is derived from the model proposed in [22], which uses a set of nonlinear equations to describe the shape of the continuum structure as a function of several parameters, including external loading, tendon routing, tendon-backbone interaction, tendon elasticity, and tendon displacement.

For the multi-point constraint system, the model in [22] can be extended by integrating multi-point constraints as a boundary condition and considering each tendon tension as a variable. The model employs the same notation and conventions as the previously described static model for consistency. The multi-point constraint requires modifications to the tendon-backbone interaction of the preceding static model, given that some tendons are attached in the middle of the robot's structure. Furthermore, the input must be altered by describing tendon displacement using capstan rotation.

Considering there are a total number of K tendons attached inside the continuum structure, with an attached constraint point position $s = \lambda_k$, the force $\boldsymbol{F}$ and torque $\boldsymbol{L}$ generated by the tendons to the constraint point can be described as

$$\begin{aligned} \boldsymbol{F}_k &= -\tau_k \frac{\dot{\boldsymbol{p}}(\lambda_k)}{\|\dot{\boldsymbol{p}}(\lambda_k)\|} \\ \boldsymbol{L}_k &= -\tau_k (R(\lambda_k)\boldsymbol{r}_k(\lambda_k))^{\wedge} \frac{\dot{\boldsymbol{p}}(\lambda_k)}{\|\dot{\boldsymbol{p}}(\lambda_k)\|}, \end{aligned} \quad (3)$$

where $k = 1, 2, 3, ...K$, τ_k is the internal tendon tension of tendon k, $\dot{\boldsymbol{p}}$ is the derivative character of backbone central line position $\boldsymbol{p}$ with respect to s, R is the material orientation of the backbone, $\boldsymbol{r}_k$ is the vector pointing from the local frame origin to the position of tendon i on the rod cross-section.

The above forces and torques can be integrated into the model by changing the initial force $\boldsymbol{m}$ and torque $\boldsymbol{n}$ of the backbone:

$$\begin{aligned} \boldsymbol{m}(\lambda_k^-) &= \boldsymbol{F}_k + \boldsymbol{m}(\lambda_k^+) \\ \boldsymbol{n}(\lambda_k^-) &= \boldsymbol{L}_k + \boldsymbol{n}(\lambda_k^+), \end{aligned} \quad (4)$$

Since the tendons are actuated using rotary capstans, considering there are a number of m sets of tendons in the robot, for each set of tendons there are n tendons, the displacement of each tendon can be derived from capstan rotation as:

$$q_{tendon_{ij}} = d_{ij}q_j. \quad i = 1, 2, 3, ...n, \quad j = 1, 2, 3, ...m \quad (5)$$

where d_{ij} is the diameter of the wheel attached to the tendon i in the tendon set j , q_j is the rotation angle for the tendon set j. The modified equations can be solved using the same solver algorithm which has been proposed in [22].The input of the algorithm, which is the displacement of each tendon q_{tendon}, can be acquired from the above equation.

B. Design and Fabrication

In this work, a TDCR demonstrator with three constraints and two degrees of freedom was built. The demonstrator is actuated by three identical actuating units to obtain omni-directional bending. Each actuation unit consists of servo motor (DS5160SSG, $60\,\mathrm{kg\,cm}$ torque, $7.4\,\mathrm{V}$, $270°$ rotation) and an attached multi-diameter capstan. The capstan consists of three wheels with a diameter of $13.2\,\mathrm{mm}$, $26.4\,\mathrm{mm}$ and $39.6\,\mathrm{mm}$ respectively. Three tendons were fixed to the three wheels for each capstan and guided through a pulley system towards the continuum robotic structure with a length of $240\,\mathrm{mm}$.

For the implementation of the multi-constraint feature, constraints were evenly distributed along the length of the continuum robotic structure with 12 amount of spacer disks. Three sets of actuating tendons (7×7 stainless steel rope, diameter: $0.4\,\mathrm{mm}$) were attached to the corresponding constraints, equally surrounding the central backbone (Ni-Ti). All tendons in the same tendon set shared the same routing channel. The routing angle of the three sets of tendons is $\pi/3$, π and $5\pi/3$, respectively.

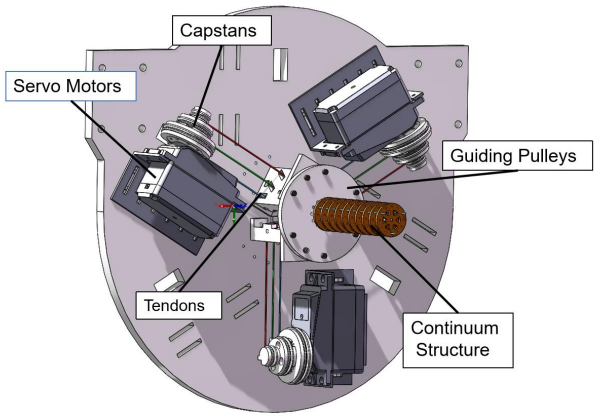

Fig. 4. 3D model of the demonstration system, overview of the design where the drive unit consists of a servomotor and capstan.

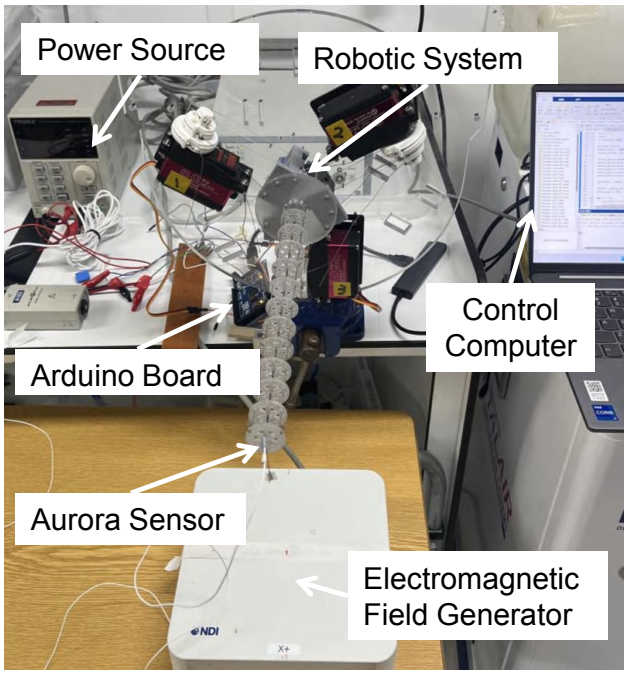

Fig. 5. Experimental setup with the robot demonstrator and the electromagnetic tracking system.

The disks were fabricated using photopolymerization-based 3D printing, while the capstans and the pulley structures were produced through fused deposition modeling (FDM) with PLA filament. The system is controlled by an Arduino board (Mega 2560, Arduino, Italy) and powered by a 7.4 V power source. The parameters for the system are detailed in Table I.

III. Experimental Evaluation

In order to verify the static model and validate the ability in stiffness strengthening of the proposed concept, the fabricated demonstrator was experimentally evaluated.

A. Tip Loading with Variable Constrain Points

Tip loading tests were carried out to compare stiffness with different numbers of constraint and to verify the static model. The experimental setup is shown in Figure 5.

The continuum structure was positioned horizontally and a lightweight plastic bag was attached to the tip to carry load. A electromagnetic tracking system based on a field generator was utilized to measure the position of the robotic tip during the experiment (Aurora, 6DOF sensortip, NDI Co., Canada). According to the Aurora system's manufacturer (NDI Co.), the 6DOF sensor tip used in our setup achieves a positional accuracy of approximately 0.48 mm RMS under typical laboratory conditions. The robot's control and data acquisition from the Aurora sensing device were achieved using MATLAB.

The electromagnetic sensor was attached to the tip of the robot, while the electromagnetic field generator was placed horizontally under the continuum structure. Before the experiments, the position of the robot base was first measured with the electromagnetic sensor for calibration. The experimental setup and calibration process were kept the same for each set of experiments. Three sets of experiments were performed with changing number of constraints. Each set of experiments is repeated three times.

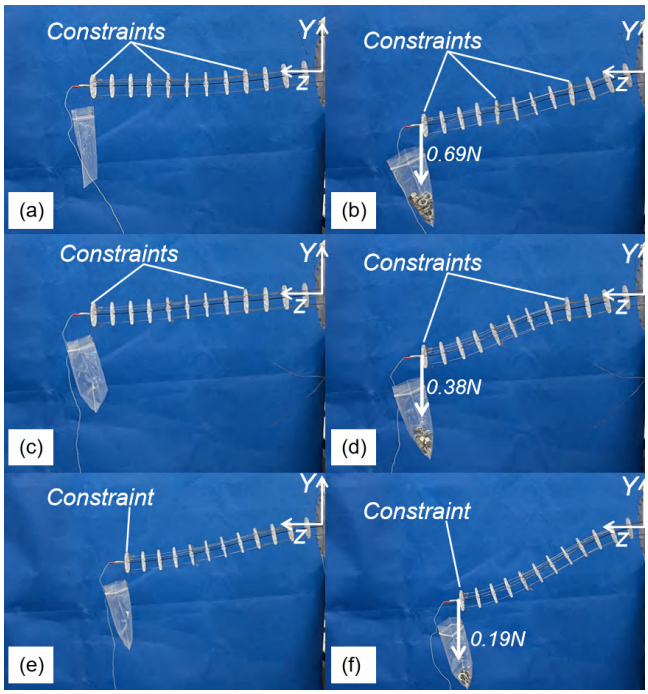

Fig. 6. Experiment results in tip loading with different constraint point settings. (a), (c) and (e) is the original shape of the continuum structure with three, two and one constraint respectively. (b), (d) and (f) is the deformed shape of the continuum structure subjected to the corresponding maximum tip loading force with three, two and one constraint respectively.

In the first set of experiments, all three constraints were applied with all nine tendons attached to the capstans. Prior to the experiment, the continuum structure was kept straight by adjusting the tendon displacement and holding the robot

TABLE I

PARAMETERS OF THE DEMONSTRATOR SYSTEM

Property	Value	Property	Value
Backbone Diameter	1×10^{-3}m	Structure Length	0.24m
Backbone Young's Modulus	7.1×10^{4}MPa	Structure Weight	1.6×10^{-2}kg
Backbone Shear Modulus	2.54×10^{4}MPa	Gravitational Acceleration	9.81m/s^2
Disk Spacing	2×10^{-2}m	Length of Tendons attached to The 1^{st} Constraint	0.416m
Disk Radius	1×10^{-2}m	Length of Tendons attached to the 2^{nd} Constraint	0.336m
Disk Thickness	1×10^{-3}m	Length of Tendons attached to The 3^{rd} Constraint	0.256m
Tendon Elasticity	1.77×10^{4}N/m		

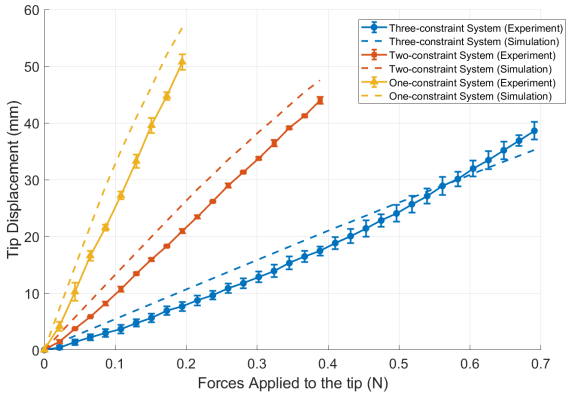

Fig. 7. Tip displacement under tip loading across different constrain point settings of experimental evaluation (solid) and simulation (dashed).

to avoid perturbations due to internal gravity. In the initial phase, the shape of the robot was deformed by internal gravity. A total of 32 M5 nuts (each weighting approximately 2.2 g) were then gradually inserted into the plastic bag to create a concentrated force at the tip along the $-y$ direction. The position of the tip was continuously recorded while the nuts were inserted into the bag. The experiment ended when all nuts had been inserted into the bag, generating an external force of 0.69 N at the tip. The deflection along the loading direction was approximately 38.5 mm, which is 16% of the total length of the continuum structure. All the nuts were then gradually retracted.

In the second set of experiments, two constraints were applied, with the tendons for the second constraint being detached from the capstan. A similar pre-test and test procedure was used as in the first set of experiments. However, the total number of nuts was reduced to 17 due to the reduction in robot stiffness, which nonetheless produced a similar deflection for comparison.

In the third set of experiments, only the first constraint point was applied. A similar experiment process was conducted with a total 8 nuts for loading. The shapes of the robot in the initial and loaded states with different constrain settings are shown in Fig 6. It can be observed from the experimental result that the robot body between the constraint points has been deformed into an 'S' shape. A robot base frame is mounted at the base of the continuum structure, with the Z axis parallel to the backbone and the Y axis in the vertical direction to describe the deflection results.

The comparison between experimental and simulated outcomes for systems with one, two, and three constraints is presented in Fig. 7. Solid lines illustrate the experimental results, with error bars indicating variations across repeated trials. In contrast, the simulated outcomes derived from the proposed static model are represented by dashed lines. The results given are aligned by presenting the relative deflection during tip loading by setting the shape under internal gravity as initial stage.

The maximum load (0.194 N) resulted in a deflection of 50.75 mm for the single constraint point system. In contrast, the systems with two and three constraint points exhibited deflections of 20.95 mm and 7.67 mm under the same load, respectively, amounting to only 41% and 15% of the deflection observed in the single constraint point system.

B. Open-Loop Control with Variable Constrain Points

A further test was conducted to demonstrate the influence of the constraint points on tip position control. Motion tests based on open-loop kinematic models were performed with three constraint point settings. Under each constraint point setting, the robot was controlled to move in a circular tip trajectory with a fixed tip orientation of $\pi/4$ and $\pi/3$ respectively. Each configuration of experiments was conducted three times and average points positions are calculated. The rotation value of the actuators was derived from the aforementioned inverse kinematic model (Sec. II-A.1). Due to the limitation of the minimum actuator rotation angle of the motor of 1.8°, the trajectory where the tip orientation is $\pi/4$ is discrete into 200 intermediate positions. And 100 intermediate positions for the trajectory with $\pi/4$ tip orientation are used to derive the rotation value.

The experimental results is shown in Fig. 8. As the number of constraint points increases, the robot's tip motion more closely approximates the expected circle. In the $\pi/3$ scenario, changing from a three-constraint system to a one-constraint configuration raised the mean error from 34.5 mm to 50.6 mm, as shown in Fig. 8. A similar trend is observed for the $\pi/4$ circle, where the mean error increased from 32.9 mm to 50.2 mm across different configuration systems.

C. Tendon tensions of systems with different constraint setting during actuation

The tendon tensions of systems with different constraint settings are compared to analyze the effect of multiple

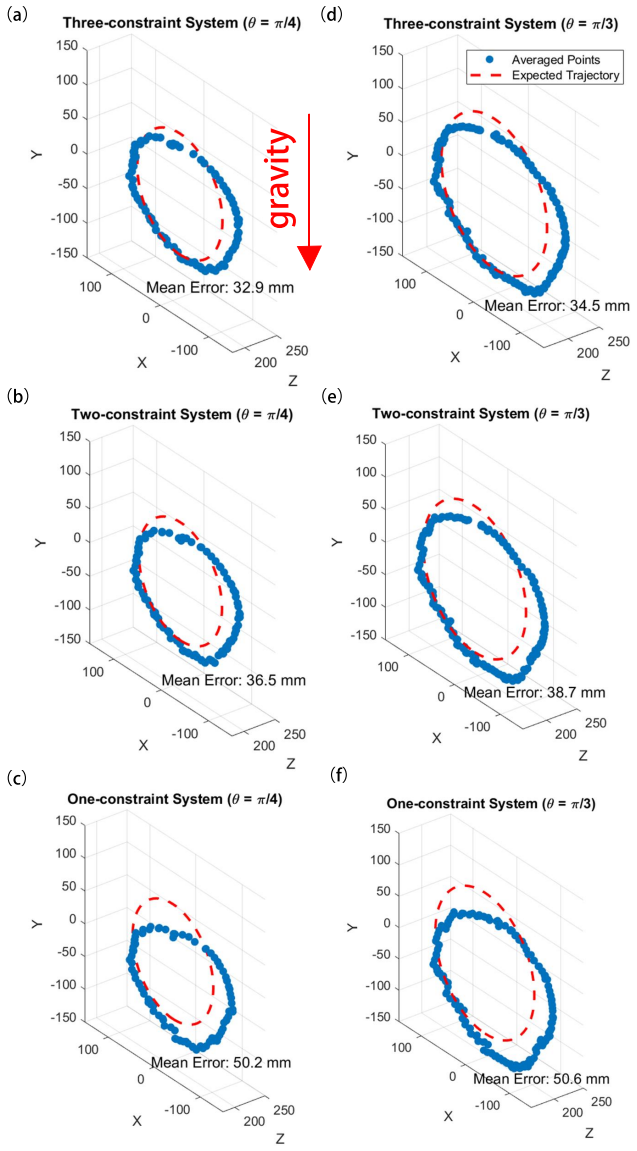

Fig. 8. Measured (blue markers) versus modeled (red dashed curve) tip trajectories of the continuum structure under one, two, and three constraint with tip orientation angles of $\pi/4$ and $\pi/3$. Mean error is calculated between the experiment trajectory and expected trajectory.

constraints during actuation. The simulation was carried out using the proposed static model, with parameters consistent with those of the experimental setup. The robot system was simulated with the aforementioned three constraint settings. During the simulation, the tendons were pulled and released gradually to actuate the robotic segment to bend from the straight stage to a curved stage with a tip orientation of $\pi/4$. This process was divided into 10 steps, with the bending angle increasing by $\pi/10$ within each step. The bending plane was set to $\varphi = 0$. For each desired bending angle of the segment, the corresponding tendon displacement values for pulling and releasing were derived from the aforementioned kinematic model. Due to the elasticity of the tendons, in each constraint setting, only the tendons with a routing

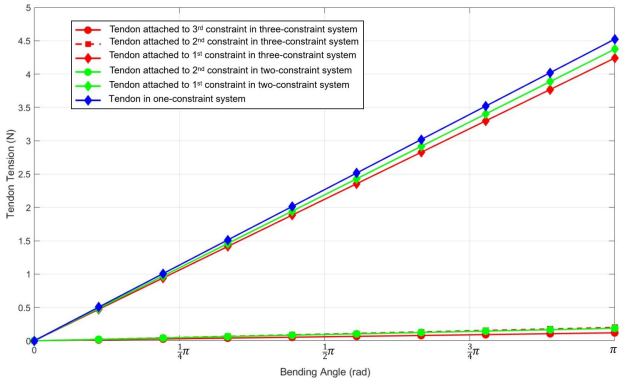

Fig. 9. Simulation results on tensions of tendons attached to different constraint points across different constraint point settings.

angle of $\alpha = 0$ were tensioned while the other tendons were in slack stage. Fig. 9 shows the simulation results of the relationship between the desired segment bending angle and the tension value of each tensioned tendon in the three constraint settings. The results show that during the actuation process, the tension values of all tendons in the multi-constraint settings are lower than in the single-constraint setting, and that all tendons connected to the tip of the segment in those three settings have similar tension values. Tensions decrease in order from the one-constraint system to the three-constraint system. However, other tendons in the multi-constraint settings remain in a relatively low-tension state during actuation.

D. Discussion

the experiments exhibit strong repeatability. The results of the tip loading experiment show a noticeable improvement in the stiffness of the robotic system with multi constraint compared to conventional system. The stiffness ratios that can be derived from the relationship between deflection and load, between the three-point constrained system, two-point constrained system and one-point constrained system are 6.6 : 2.7 : 1 under a similar load.

Simulations closely align with experimental results for all configurations, validating the model's accuracy, with an average error of $2.36\,\mathrm{mm}$ and a maximum error of $7.85\,\mathrm{mm}$, representing 1.29% and 3.3% of the total length of the continuum structure. This shows good reliability and accuracy of the static model. A major possible source of error is the friction between tendons and spacer disks, which allows a higher stiffness value than predicted by preventing relative movement between tendons and disks.

The effectiveness of the kinematic model is confirmed through open-loop control experiments with circular trajectories. The control accuracy in both experimental tip trajectories improves with the increment of constraint points with a reduction of error of 34.5% and 31.8% for the trajectory with a tip orientation of $\pi/3$ and $\pi/4$, respectively. The results demonstrate the ability of multi constraint to improve the control accuracy of the TDCR. Further more, these results indicate that our multi constraint system enhances stability

and reduces compliance, enabling the robot to resist external forces, such as gravity, more effectively and achieve greater precision.

The verification of the static model in experiments guarantees the simulation results. Tendons from both multi-constraint systems have lower tension values throughout the entire actuating process than that from single-constraint system. It can be seen that the tendons connected to the tip of the structure in all three constraint systems have similar tension values, while the tension values of the other tendons are significantly lower. This can be explained by the effectiveness of the inverse kinematic model based on constant curvature and tendon elasticity. It can be concluded that the tendon tension level can be maintained at a similar level to that of the single-constraint system during actuation of the continuum segment.

However, only the lateral stiffness improvement was demonstrated in the above experiments. The axial stiffness was not addressed in this work.

IV. Conclusion

This paper presented the concept of multi constraint for TDCR to increase the structure stiffness without compromising in increasing tendon tensions and limiting motion ability, which is a major defect for existing stiffen strategies. The relevant design criteria were proposed together with a kinematic and static model. A multi-constraint experimental platform was designed and fabricated for experimental evaluation. The experimental results of the tip loading experiment and the kinematic model control experiment show a significant improvement in structure stiffness and motion accuracy, respectively, by implementing multi constraint for TDCR. The accuracy of the static model was verified by comparison with experimental results. And simulation in tendon tensions during actuation process was conducted to demonstrate the ability of tension maintenance compared with original system.

The concept of multi constraint can be implemented to novel TDCR systems by considering the proposed system schematic. It can be controlled by the kinematic model, while the static model can be used as a design tool to determine the ideal stiffness and tendon tension value by designing the constraint settings. The robot with multi constraint is expected to realize programmable stiffness change during manipulation by attaching and detaching constraint tendons.

The concept of multi constraint may find relevant applications in TDCR, which requires working with both compliant and stiffened states in confined and small space, and further expand the application area of TDCR. Future work includes exploiting the ability in torsional stiffness strengthening using multi constraint implementation in clinical scenario and mechanisms for changing stiffness automatically.

V. Acknowledgment

The authors want to thank Ziqi Yang and Libaihe Tian from Imperial College London for their help in experiment.

References

[1] M. Hwang and D.-S. Kwon, "Strong continuum manipulator for flexible endoscopic surgery," *IEEE/ASME Transactions on Mechatronics*, vol. 24, no. 5, pp. 2193–2203, 2019.

[2] M. Wang, X. Dong, W. Ba, A. Mohammad, D. Axinte, and A. Norton, "Design, modelling and validation of a novel extra slender continuum robot for in-situ inspection and repair in aeroengine," *Robotics and Computer-Integrated Manufacturing*, vol. 67, p. 102054, 2021.

[3] Z. Wang, N. M. Freris, and X. Wei, "Spirobs: Logarithmic spiral-shaped robots for versatile grasping across scales," *Device*, p. 100646, 2024.

[4] A. L. Orekhov, E. Z. Ahronovich, and N. Simaan, "Lie group formulation and sensitivity analysis for shape sensing of variable curvature continuum robots with general string encoder routing," *IEEE Transactions on Robotics*, vol. 39, no. 3, pp. 2308–2324, 2023.

[5] R. Pfeifer, M. Lungarella, and F. Iida, "Self-organization, embodiment, and biologically inspired robotics," *Science*, vol. 318, no. 5853, pp. 1088–1093, 2007.

[6] J. A. Childs and C. Rucker, "Leveraging geometry to enable high-strength continuum robots," *Frontiers in Robotics and AI*, vol. 8, 2021.

[7] Y. Sun and T. C. Lueth, "Enhancing torsional stiffness of continuum robots using 3-d topology optimized flexure joints," *IEEE/ASME Transactions on Mechatronics*, vol. 28, no. 4, pp. 1844–1852, 2023.

[8] J. Ahn, M. Hwang, D. Kong, J. Kim, and D.-S. Kwon, "Asymmetric rolling contact joint for enhanced payload capabilities," *IEEE/ASME Transactions on Mechatronics*, vol. 29, no. 1, pp. 202–213, 2024.

[9] K. Mizushima, T. Oku, Y. Suzuki, T. Tsuji, and T. Watanabe, "Multi-fingered robotic hand based on hybrid mechanism of tendon-driven and jamming transition," in *2018 IEEE International Conference on Soft Robotics (RoboSoft)*, 2018, pp. 376–381.

[10] W. Wang, C. Y. Yu, P. A. Abrego Serrano, and S.-H. Ahn, "Shape memory alloy-based soft finger with changeable bending length using targeted variable stiffness," *Soft Robotics*, vol. 7, no. 3, pp. 283–291, 2020, pMID: 31750782.

[11] M. Mattmann, C. De Marco, F. Briatico, S. Tagliabue, A. Colusso, X.-Z. Chen, J. Lussi, C. Chautems, S. Pané, and B. Nelson, "Thermoset shape memory polymer variable stiffness 4d robotic catheters," *Advanced Science*, vol. 9, no. 1, p. 2103277, 2022.

[12] P. Rao, C. Pogue, Q. Peyron, E. Diller, and J. Burgner-Kahrs, "Modeling and analysis of tendon-driven continuum robots for rod-based locking," *IEEE Robotics and Automation Letters*, vol. 8, no. 6, pp. 3126–3133, 2023.

[13] H. Wang, Z. Chen, and S. Zuo, "Flexible manipulator with low-melting-point alloy actuation and variable stiffness," *Soft Robotics*, vol. 9, no. 3, pp. 577–590, 2022, pMID: 34152857.

[14] K. Oliver-Butler, J. Till, and C. Rucker, "Continuum robot stiffness under external loads and prescribed tendon displacements," *IEEE Transactions on Robotics*, vol. 35, no. 2, pp. 403–419, 2019.

[15] P. Molaei, N. A. Pitts, and H. B. Gilbert, "Independent tendons increase stiffness of continuum robots without actuator coupling," in *2023 IEEE/ASME International Conference on Advanced Intelligent Mechatronics (AIM)*, 2023, pp. 72–78.

[16] Y.-J. Kim, S. Cheng, S. Kim, and K. Iagnemma, "A stiffness-adjustable hyperredundant manipulator using a variable neutral-line mechanism for minimally invasive surgery," *IEEE Transactions on Robotics*, vol. 30, no. 2, pp. 382–395, 2014.

[17] Y. Cai, A. L. Orekhov, and H. Choset, "Statics modeling of discrete joint surgical probes with tendon-based stiffening," in *2023 International Symposium on Medical Robotics (ISMR)*, 2023, pp. 1–7.

[18] B. Jones and I. Walker, "Kinematics for multisection continuum robots," *IEEE Transactions on Robotics*, vol. 22, no. 1, pp. 43–55, 2006.

[19] M. Moradi Dalvand, S. Nahavandi, and R. D. Howe, "General forward kinematics for tendon-driven continuum robots," *IEEE Access*, vol. 10, pp. 60 330–60 340, 2022.

[20] M. M. Dalvand, S. Nahavandi, and R. D. Howe, "An analytical loading model for n -tendon continuum robots," *IEEE Transactions on Robotics*, vol. 34, no. 5, pp. 1215–1225, 2018.

[21] D. C. Rucker and R. J. Webster III, "Statics and dynamics of continuum robots with general tendon routing and external loading," *IEEE Transactions on Robotics*, vol. 27, no. 6, pp. 1033–1044, 2011.

[22] Z. Du and W. Bai, "Tendon-driven continuum robot stiffness with pretension effect," in *IECON 2023- 49th Annual Conference of the IEEE Industrial Electronics Society*, 2023, pp. 1–6.